Available online at www.sciencedirect.com

ScienceDirect

Physics Procedia 3 (2010) 615–625

Physics Procedia

www.elsevier.com/locate/procedia

International Congress on Ultrasonics, Universidad de Santiago de Chile, January 2009

Improved image quality with new ultrasound imaging techniques

C. Fritsch[a]*, J. Camacho[a], M. Parrilla[a]

[a]*Instituto de Automática Industrial, CSIC, La Poveda (Arganda),28500 Madrid, Spain*

Abstract

This work addresses three key subjects to the image quality with phased arrays: timing accuracy, beamforming strategy and post-processing for increased resolution and suppression of grating and side lobes.
Timing accuracy is achieved by defining a modular and scalable architecture which guarantees timing errors of a few tens of picoseconds, whatever is the system size. The proposed beamforming methodology follows the progressive focusing correction technique, which keeps low focusing errors, provides a high information density and has a simple implementation for real-time imaging. Then, phase coherence imaging is defined to suppress grating and sidelobe indications and increasing the lateral resolution.

Keywords: Beamforming; Dynamic Focusing; Phase Coherence Imaging; Progressive Focusing Correction

1. Introduction

Ultrasonic imaging is a standard technique in the medical field and is being rapidly adopted by the NDE community. But phased array real-time beamforming is a challenging process. It involves acquiring and processing data from tens to thousands of channels at several MS/s. A digital beamformer produces a vector s_i of output samples from the M samples r_{ik} received by the N array elements ($1 \le i \le M$, $1 \le k \le N$). It performs a simple operation (summation) on accurately delayed samples at very high speed (several GS/s). For dynamic depth focusing, a different delay τ_{ik} is required to compensate the time of flight of echoes from every point i in the imaged space to every array element k:

$$s_i = s(iT_S) = \sum_{k=1}^{N} r_i(iT_S + \tau_{ik}), \qquad (1)$$

* Corresponding author: Carlos Fritsch. Tel.: +3491-871-19-00; fax: +3491-871-70-50.
E-mail address: carlos@iai.csic.es.

doi:10.1016/j.phpro.2010.01.078

where TS is the sampling period and τik is continuous. In practice, τik is digitized with certain time-resolution, leading to delay-quantization lobes [1]. The rms delay-quantization lobe to the main lobe amplitude ratio is:

$$\eta \approx \frac{\pi}{\mu\sqrt{6N}} \quad \mu >> 1 \tag{2}$$

where μ is the relation of the received signal period (TR=1/fR) to the delay time resolution (TX). To achieve a η value below half the theoretical dynamic range:

$$\mu \geq 2\pi\sqrt{\frac{N}{6}} \tag{3}$$

This yields μ > 29 for a 128-element linear array. Oversampling the received data is not practical due to cost, power consumption and data volume reasons. A notable exception is the use of Sigma-Delta (SD) modulators, which provide a serial data stream and performs the beamforming process at a high sampling rate [2]. However, most digital beamformers acquire signals at the Nyquist rate and use different approaches to reach the required timing resolution [3].

On the other hand, in large channel-count systems, strict timing coherence must be kept over the whole system. This requirement is of particular importance when designing scalable beamforming systems to adapt the electronics to the application needs, from tens to thousands of elements [4].

Image quality is also affected by the sidelobe level and –in some cases– by grating lobes. This is especially important with 2D arrays, where sparse apertures are frequently used to reduce the otherwise excessive channel-count [5]. Significant image quality improvements require addressing these subjects.

This work presents a set of new techniques to overcome these problems. The AMPLIA architecture designed for scalable and tight-timing ultrasound imaging is described in Section 2. Section 3 proposes the Progressive Focusing Correction (PFC) beamforming technique and its implementation. Section 4 addresses a preliminary study of Phase Coherence Imaging to improve the image quality beyond the limits provided by conventional phased array imaging. Simultaneous suppression of side and grating lobes is achieved together with improvements in lateral resolution, enhancing the image contrast and detail identification.

2. The AMPLIA architecture

2.1. Topology

AMPLIA has a branched pipeline structure, based on 3 components (Fig. 1):

- The Interface and Control Unit (ICU).
- The bidirectional 32-bit data AMPLIA bus.
- Processing Modules (PM).

The ICU performs the transactions between a host computer and the AMPLIA bus. It stores data results and command programs to operate the system independently of the host, achieving a predictable timing. Commands are issued by the ICU to the system; results are stored in the ICU and, then, transferred to the host computer.

The segmented AMPLIA bus has 32-bit data and 8 control lines. Data provided by PMs are validated by an active-low level on the /DAV signal. Data sent by the ICU are qualified by the state of TC<1:0> (addressing, reading, writing or idle). The direction is also indicated by the UAS line. Two signals (PRG, RST) control the initialization tasks. A rising edge on the RUN line starts an acquisition and processing cycle, which is normally terminated by the system by lowering the bidirectional TC<0> line. Parameter programming and other tasks are

mastered by the ICU while RUN is low. The clock CKS synchronizes all the transactions. Data pass from module to module in both directions, introducing a latency of one clock cycle. Processing Modules can be:

Branch PMs that have 2 ports connecting to adjacent PMs.
Node PMs that have 3 ports: two of them connect to adjacent node PMs or to the ICU; the third one is tied to a chain of branch PMs.

Static addresses to node PMs are multiple of 8 (i.e. 0, 8, 16 ...). Branch PMs are assigned sequential addresses following that of their parent node-PM (i.e. 1, 2, 3 ... or 9, 10, 11 ...). A large system can be built with up to 256 modules. Broadcast addresses can be also assigned to user selected modules, which execute simultaneously.

Broadcast commands simplify and accelerate tasks and play an important role in keeping timing coherence. Following a low-to-high transition in the RUN line (*start event*), the system enters the processing state. The RUN signal is delayed by the latency introduced at every module. A compensation mechanism synchronizes the start event in all the PMs within a few tens of picoseconds, as it is described later.

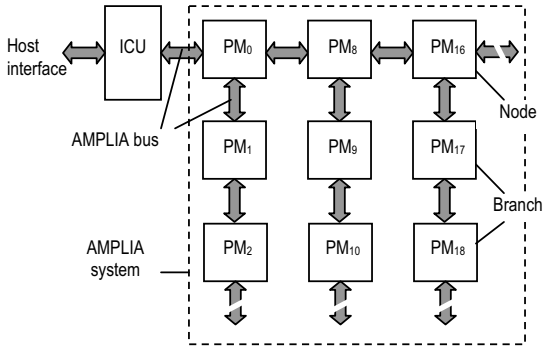

Fig.1 Structure of the AMPLIA architecture

In the processing state, every module acquires and processes data from its own channels, receives results from the precedent module in the chain and outputs the combined results to the next one. This way, all the processing modules perform at the same sustained rate of the system clock. Increasing the number of channels is a matter of increasing the number of processing modules. FIFO memories help to synchronize the differences in the acquisition instants and the production of results by every module.

2.2. Achieving timing coherence

A key feature of AMPLIA is its capability of keeping timing coherence along a large system with many processing modules. In spite of the relatively low system clock frequency (40 MHz), synchronized operations are executed within a few tens of picoseconds along the whole system by implementing two mechanisms:

a) A coarse time resolution of one system clock period is achieved by re-synchronizing all bus signals, including the clock. Commands propagate through the whole system, adding 1 cycle of delay for every PM.
b) Digital Clock Managers (DCMs) in FPGAs [6] are used in a feedback loop to keep in phase the input and output clocks of every PM, within a few tens of picoseconds. The same clock is accurately seen by all the configured modules, independently of the system size, capacitive loading, etc.

To compensate the latency introduced by every module, an enumeration process is followed during start-up. The ICU broadcasts an *addressing command* to all the modules in the system with two data fields: ADDR=0 and

DLY=*Y*, where *Y* is the maximum latency in the current configuration. Every module sets its own address to the value received from the precedent one and propagates the command to the next module after modifying the ADDR field to ADDR+1 or ADDR+8 (depending of the port). This way, static addresses are automatically assigned to all the modules in the system. Simultaneously, every module sets its own DLY value to that received from the precedent module, and propagates the value DLY minus 1 to the next one in the chain. All the modules use the stored DLY value to delay that number of clock cycles the execution of any command to compensate the latency. Broadcast commands and the start event simultaneously execute in the whole system.

3. The Progressive Focusing Correction technique

The Progressive Focusing Correction technique (PFC) is a dynamic depth focusing method that exploits two characteristics common to phased array imaging:

a) The differences in the echo arrival times from consecutive foci in a given steering direction to an element asymptotically tend to the time of flight among foci as the range increases.
b) The depth of focus increases with range.

3.1. Coding the focusing delays.

Let it be a linear array of N elements at $(x_k, 0)$ $1 \le k \le N$ and foci located on a ray starting at the array centre at (0, 0) with a steering angle θ. The round trip time from the origin to a focus at (R_i, θ) and to the element at $(x_k, 0)$ in a medium with propagation velocity c is:

$$T_{ik} = \frac{1}{c}\left(R_i + \sqrt{R_i^2 + x_k^2 - 2R_i x_k \sin\theta}\right) \tag{4}$$

Let T_S be the sampling period that verifies the Nyquist criterion and T_X the time resolution required by (3). It is convenient that $T_S = \nu T_X$, with ν integer. Samples are regularly distributed at intervals ΔR:

$$\Delta R = \frac{cT_S}{2} = \frac{c\nu T_X}{2} \tag{5}$$

The echo arrival time difference to the element k from two consecutive foci at (R_i, θ) and $(R_i+\Delta R, \theta)$ is obtained from (4) and substitution of (5):

$$\Delta T_{ik}(R_i, \theta) = \left(1 + \frac{R_i - x_k \sin\theta}{\sqrt{R_i^2 + x_k^2 - 2R_i x_k \sin\theta}}\right)\frac{\nu T_X}{2} \tag{6}$$

This function is independent of c and asymptotically tends to νT_X when $R_i \to \infty$. Thus, there is some range R_0 from which:

$$(\nu - a)T_X \le \Delta T_{ik} \le \nu T_X, \quad R_i \ge R_0 \tag{7}$$

where $a < \nu$. Choosing a=1, the value of ΔT_{ik} will remain between ν-1 and ν for $R_i \ge R_0$. The discrete time differences are obtained with a time resolution T_X as:

$$\Delta T_Q(i,k) = \left|\frac{\Delta T_{ik}}{T_X}\right|_{\uparrow\downarrow} > 0 \tag{8}$$

where $|\cdot|_{\uparrow\downarrow}$ denotes the rounding function. For $R_i \ge R_0$, $\Delta T_Q(i, k)$ will take only the values ν or ν-1. Thus,

$$Q(i,k) = \nu - \Delta T_Q(i,k), \tag{9}$$

represents the single-bit *focusing code*. The value of Q indicates if the sampling instant for sample i in channel k should be advanced (Q =1) or not (Q =0) by a quantum time T_X to get it in focus. This ensures that the sampling instants will differ, at most, by $T_X/2$ from the exact value.

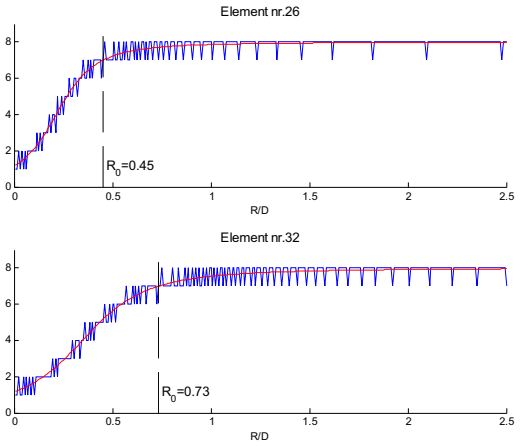

Fig.2 Continuous (red) and discrete (blue) differences normalized to T_X.on the arrival time from consecutive foci, for elements 26 and 32, θ=45º and v=8. Range R normalized to D.

Fig. 2 shows an example for elements 26 and 32 of a 32-element array, $d=\lambda/2$, steering angle θ=45º, v = 8 and a sampling frequency $f_S=4f_R$. The continuous values (in red) are the normalized differences $\Delta T_k/T_X$ of the echo arrival times to element k from depths R/D (D=aperture size=Nd), obtained by differentiation of (4). The value $\Delta T_Q(k)$ (in blue) is given by (8). The timing error is always below $T_X/2$. The minimum normalized ranges R_0 are 0.45 and 0.73 for elements 26 and 32, respectively. From these ranges and ahead, the discrete differences oscillate between v-1=7 and v=8, condition expressed by (7) with a=1, and the focusing codes Q oscillate between 1 and 0.

Fig. 3 shows a fragment of the 1-bit/focus memory obtained from (9) for channels 16 to 32. The zero-valued part at the lowest ranges (in red) indicates the region where more than 1 bit would be required to express the focusing code.

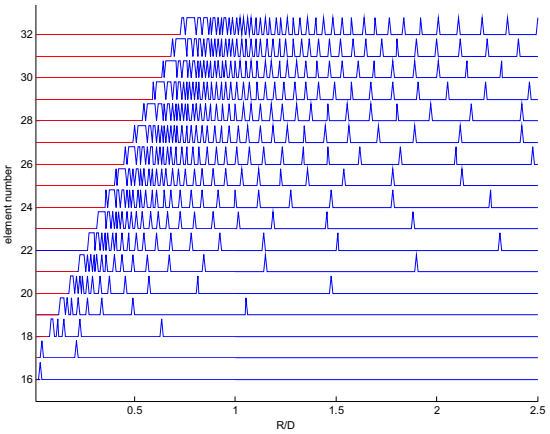

Fig.3 Fragment of the 1-bit/focus focusing memory for elements 16 to 32 and a steering angle of 45º.

3.2. Increasing the information density.

The PFC technique provides a good focusing information density: all the samples can be dynamically focused just using 1 bit per sample. But this can be further improved by dynamically changing the distance among foci, as the focus depth increases with range.

To this purpose the imaging range is divided in sections with a *progressively* increasing number of samples between foci. This way, starting section 1 with m_1=1 (all samples are focused), section m starts at some range $R_0(m)$ with m samples between foci. The range $R_0(m)$ is given by (7) just changing v by mv.

This reduces the number of foci and Q-codes required for the imaging range. The start of section m, for m>1, is the maximum of the ranges $R_0(m)$ computed for all the channels. Section 1 may start at range 0, using the individual $R_0(1)$ values to set the dynamic aperture. Obviously, the initial range can be higher than this figure, as well as the starting value m_1.

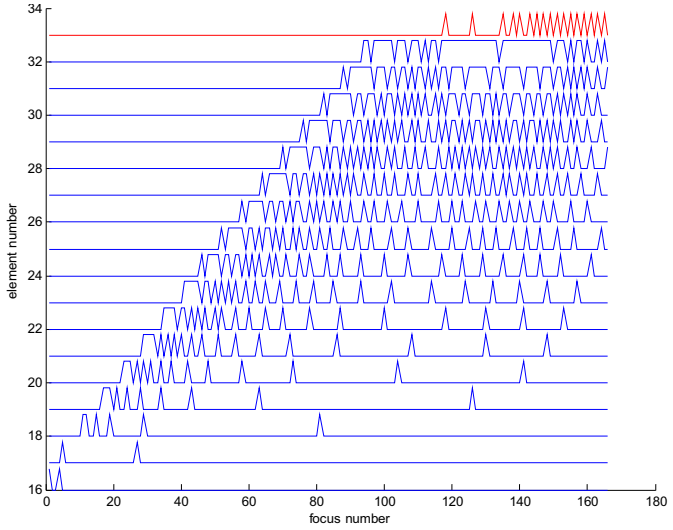

Fig.4 P-code (upper trace, 33) and Q-codes (traces 16 to 32) for PFC with dynamically changing the samples/focus from 1 to 18. Only 166 foci are required for R/D=4.

A single-bit memory, shared by all the channels, provides P-codes indicating the section breaking points. Fig. 4 shows the P-codes (upper trace, in red) and the Q-codes for imaging up to a depth R=4D (the far field limit). Only 166 foci (bits) are used, in contrast with the 512 bits required for focusing at all the samples (sampling rate $f_S = 4{\cdot}f_R$).

Furthermore, Fig. 5 shows the normalized timing error T_E at the foci for a progressive increase of m from 1 to 18. The error remains within the expected bounds of $\pm 0.5T_X$.

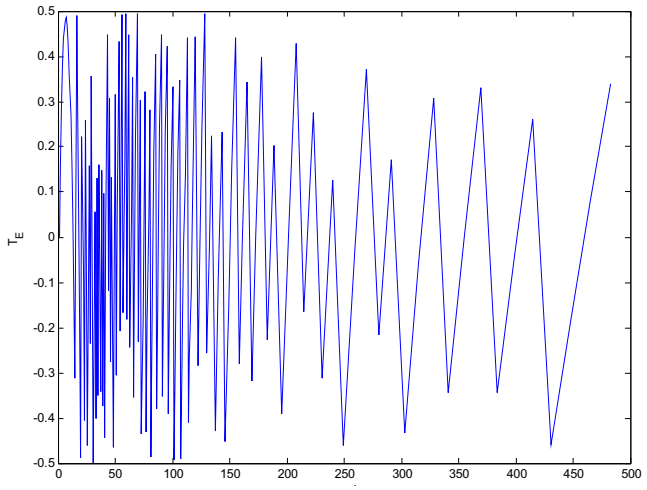

Fig.5 Progressive focusing timing error at the foci. Element 32, steering angle = -45º, sections 1 to 18, v =8.

On the other hand, Fig. 6 shows the normalized timing errors for all the acquired samples together with the starting point of each section (indicated by a small circle). It is seen that all the samples get correctly focused (within $\pm 0.5T_X$) in the first section (where m=1), and with a slightly higher error at sections with m>1. Although no Q-codes are used to focus these samples, the error is bounded and small (less than $0.8T_X$, in this case). This has little impact on the image, which is re-focused a few samples ahead. On the other hand, the number of samples per focus decreases as the section number increases, eventually reaching the lower limit of 1 focus/section.

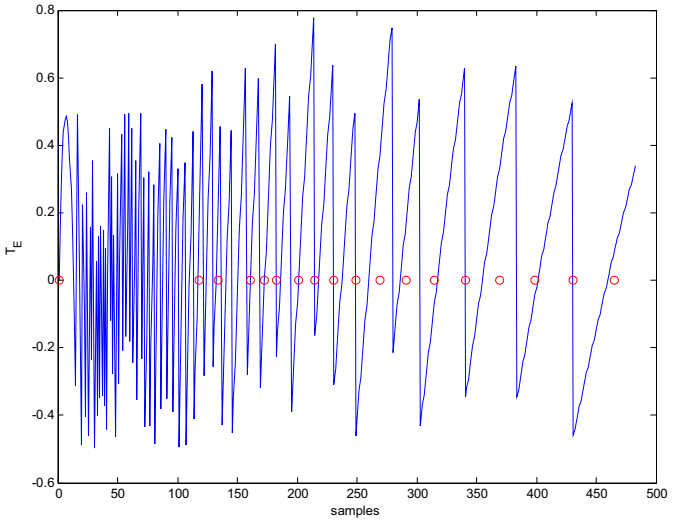

Fig.6 Progressive focusing timing error at all the samples. Element 32, steering angle = -45º, sections 1 to 18, v =8.

3.3. Adapting the PFC to simultaneous sampling

The PFC technique determines the sampling instants of the incoming echoes to get a focused aperture data. These data can be simply added to get the output samples dynamically focused with good timing resolution. Only a FIFO memory is required to synchronize the different acquisition times at different channels.

However, recent developments integrate several amplifiers and A/D converters in a chip with an efficient LVDS interface, but they share a common sampling clock. The PFC can be used as well in these cases, but now it is required to simulate the different sampling instants. This is achieved by means of interpolation.

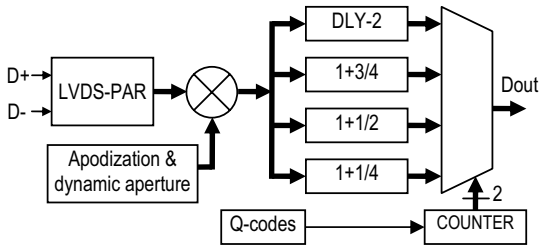

Fig.7 An interpolation scheme for using simultaneous sampling LVDS A/D converters with the PFC technique

Fig. 7 shows the working principle for v=4. First, the differential serial data stream at (D+, D-) is converted to parallel. The signal is multiplied by an apodization coefficient or by zero for dynamic aperture control. The result enters a bank of four fractional delay filters that perform the interpolation function. These FIR filters simultaneously generate four time delayed samples, differing by ¼ the sampling period T_S. A counter controls the multiplexer to select the appropriate data. If Q=0, successive samples at *Dout* are separated by one T_S. When Q=1, the counter increments and the next filter output is selected; the next sample will be taken at ¾ T_S from the precedent one, thus performing the focusing action.

4. Phase Coherence Imaging

The combination of the described techniques allows obtaining the highest quality images due to the low focusing errors achieved by the AMPLIA strict timing and by the PFC technique. In practice, the limits will be mostly determined by the array characteristics as long as the focal laws are correctly computed and programmed.

In conventional phased array imaging, the aperture size limits the lateral resolution, the main to side lobe level ratio constraints the dynamic range and, when the distance among elements is greater than $\lambda/2$, grating lobe artifacts blur the image. Addressing these shortcomings is the goal of new techniques that we are investigating. Here, the basic principles and some experimental results of *phase coherence imaging* [7] will be presented.

4.1. The phase coherence factor.

After application of the beamforming delays in a conventional phased array or the variable sampling involved with the PFC technique, the aperture data is ready to be coherently summed. In this process, only the amplitude is considered, while the aperture data phase is ignored. However, the phase of the signals may play an important role on imaging.

Phase coherence imaging analyzes the *phase diversity* along the aperture data to extract a *coherence factor* (*CF*) that measures the focusing quality, with a value between 0 and 1. The *CF* weights the coherent sum to suppress those indications coming from out of focus regions, that is, at the sidelobes or at the grating lobes.

There are as many ways to define the *CF* as phase dispersion measurement functions of the aperture data. The most evident is the standard deviation $\sigma(k)$ of the phases $\varphi_i(k)$ for $1 \le i \le N$ of the delayed signals for range k. Here, the *CF* is defined as:

$$CF(k) = \max\left[0, 1 - \gamma_0 \cdot \sigma(k)\right] \qquad (10)$$

where max(·) guarantees that $0 \le CF \le 1$ and the parameter γ_0 allows to adjust the sensitivity. If $\sigma(k)$ is high, as it happens at the sidelobes, $CF(k) \to 0$; at the main lobe, all the aperture data phases are nearly equal, $\sigma(k) \to 0$ and $CF(k) \to 1$. A very simple method has been devised to discriminate echoes coming from the main lobe against those coming from the sidelobes.
Furthermore, within the main lobe, phase diversity increases as the direction of incoming echoes separates from the steering angle. Therefore, $CF(k)$ decreases from 1 towards zero as the signal direction separates from the main lobe axis. After the weighting operation, the lateral resolution becomes improved.

At the grating lobes, the wideband signals used in ultrasonic imaging compose coherently only in a few elements, due to the reduced length of the ultrasonic pulse. In the remaining elements, phases will show a large disparity, mainly due to noise (low amplitude, but random phase). The resulting phase coherence factor will be low in these regions, where $\sigma(k)$ is high. This way, the grating lobe artifacts can be also suppressed.

5. Experimental work.

The panel of Fig. 8 shows some exemplary results of phase coherence imaging. The left column shows original images; at the right column, the corresponding images processed with phase coherence are shown. The two first rows show 60-dB images of a simulated phantom with several point-reflectors, using an N=64 element array with inter-element pitch $\lambda/2$ and dynamic focusing in reception. At the right, a neat suppression of the sidelobe indications and a simultaneous improvement of lateral resolution after phase coherence imaging can be appreciated.

For the images in the second row, the array elements were separated λ. This produces the grating lobes shown in c), hiding most of the low (-26 dB) reflectivity points. However, after phase coherence processing, these points appear (see d) with a simultaneous suppression of the grating lobe artifacts.

The third row shows 80 dB images of a cyst phantom obtained with a 3.5 MHz, 128-element array. Complete data sets for these images are provided by the University of Michigan at http://bul.eecs.umich.edu/.

Synthetic Transmit Aperture (STA) processing [8] is used to get dynamic focusing in emission and in reception. Raw data were up-sampled by 8 to avoid delay quantization lobes.

The image obtained without further processing is shown in e). The image obtained with phase coherent imaging is shown in f). It can be appreciated the increase of dynamic range and contrast, especially at the bottom-left cyst.

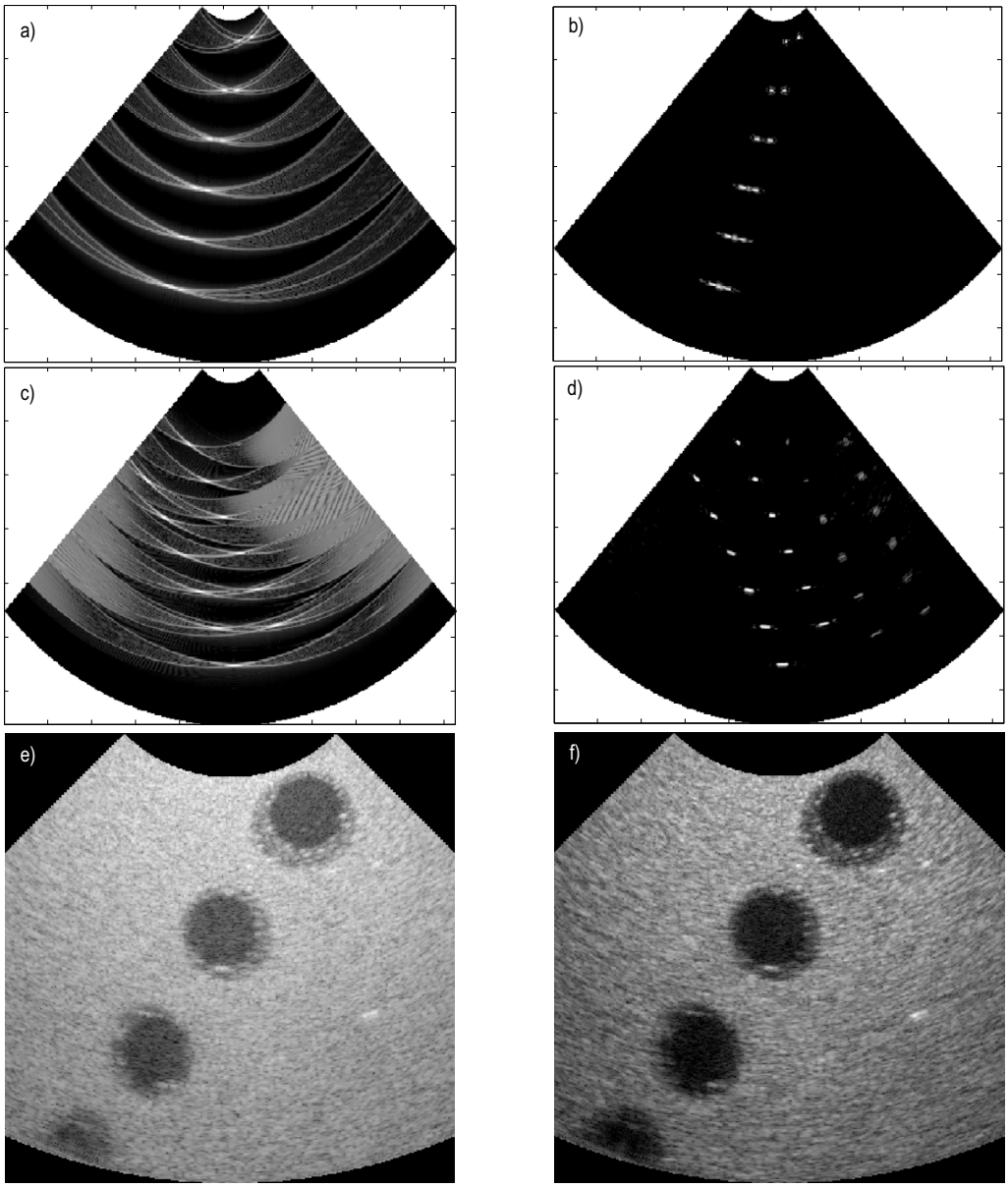

Fig.8 Left column: original; right column: corresponding phase coherence imaging. a) to d): 60-dB images of a simulated phantom of point targets, N=64; a) and b) $d=\lambda/2$, c) and d) $d=\lambda$. e), f): 80 dB images of a cyst phantom, N=128, $d=\lambda/2$.

6. Conclusions

High timing accuracy is required to achieve the full dynamic range provided by a given array. The described AMPLIA architecture yields this support with errors of a few tens of picoseconds, guaranteed by design.

The beamforming process must also keep low timing errors. This is achieved with the Progressive Focusing Correction technique for dynamic focusing in phased arrays. The *PFC* is modular, requires few hardware resources and encodes the focusing information quite efficiently. Time resolution can be chosen arbitrarily low, as a sub-multiple of the master clock period.

Both characteristics allow a further step to improve the image quality by phase coherence imaging. A phase coherence factor *CF*, which measures the focusing quality from the phase diversity shown by the aperture data, was defined. As long as timing delays are accurate, *CF* is near unity for signals coming from the focus at the main lobe axis and close to zero for echoes coming from the side or grating lobes. This offers a valuable tool to suppress these indications, with a simultaneous improvement of lateral resolution.

These results are especially important for 2D arrays, with a large number of elements and where sparse apertures with the corresponding high side and grating lobes are used to limit the complexity of the electronics.

Acknowledgements

Work supported by grant TRA 2007-67711/AUT of the Spanish Ministry for Science and Innovation.

References

[1] D. K. Peterson, G. S. Kino, "Real-time digital image reconstruction: A description of image hardware and an analysis of quantization errors", *IEEE Trans. on Sonics and Ultrasonics*, vol. 31, no. 4, pp. 337-351, 1984.
[2] M. Kozak, M. Karaman, "Digital phased array beamforming using single-bit delta-sigma conversion with non-uniform oversampling", *IEEE Trans. UFFC*, 48, 4, pp. 922-930, 2001.
[3] K. Ranganathan, M. K. Santy, T. N. Blalock, J. A. Hossack, W.F.Walker, "Direct sampled I/Q beamforming for compact and very low-cost ultrasound imaging," *IEEE Trans. UFFC.*, 51, no. 9, 1082–1094, 2004.
[4] J. L. Schwartz, B. D. Steinberg, "Ultrasparse, ultra-wideband arrays," *IEEE Trans. UFFC.*, 45, 2. pp. 376-393, 1998.
[5] G. R. Lockwood, F. S. Foster, "Optimizing the radiation pattern of sparse periodic two-dimensional arrays", *IEEE Trans. UFFC.*, 43, 1, pp. 15-19, 1996.
[6] N. Sawier, "Active phase alignment", *Xilinx XAPP-268*, Dic. 2002.
[7] C. Fritsch, M. Parrilla, J. Camacho, "Procedimiento y aparato para la corrección de imágenes ultrasónicas por análisis de fase", *Pat. P200802402*, 8 Ago 2008.
[8] K. M. Gammelmark and J. A. Jensen, "Multi-element synthetic transmit aperture imaging using temporal encoding, *IEEE Trans. Med. Imag.* 22, 4, 552-563, 2003.